

Diurnal Tides in the Arctic Ocean

Z. KOWALIK

Institute of Marine Science, University of Alaska, Fairbanks

A. Y. PROSHUTINSKY¹

Arctic and Antarctic Research Institute, St. Petersburg, Russia

A two-dimensional numerical model with a space grid of about 14 km is applied to calculate diurnal tidal constituents K_1 and O_1 in the Arctic Ocean. Calculated corange and cotidal charts show that along the continental slope, local regions of increased sea level amplitude, highly variable phase and enhanced currents occur. It is shown that in these local regions, shelf waves (topographic waves) of tidal origin are generated. In the Arctic Ocean and Northern Atlantic Ocean more than 30 regions of enhanced currents are identified. To prove the near-resonant interaction of the diurnal tides with the local bottom topography, the natural periods of oscillations for all regions have been calculated. The flux of energy averaged over the tidal period depicts the gyres of semitrapped energy, suggesting that the shelf waves are partially trapped over the irregularities of the bottom topography. It is shown that the occurrence of near-resonance phenomenon changes the energy flow in the tidal waves. First, the flux of energy from the astronomical sources is amplified in the shelf wave regions, and afterwards the tidal energy is strongly dissipated in the same regions.

1. INTRODUCTION

Measurements and tidal theories are primarily concerned with the semidiurnal tides (M_2 and S_2) whose amplitudes generally dominate over all tidal constituents. *Mooers and Smith* [1968] on the Oregon shelf and *Cartwright* [1969] off the west coast of Scotland found that in the field of velocity the reverse situation can occur, i.e., diurnal tidal currents can dominate over semidiurnal currents. This phenomenon has been found in many locations and has been identified with continental shelf waves of tidal origin [e.g., *Yefimov et al.*, 1985]. In the Arctic Ocean, local response to the tidal forcing is especially conspicuous in the diurnal range of a velocity field. *Hunkins* [1986] reported a significant topographic amplification of the diurnal tide over the Yermak Plateau, with high velocities and enhanced mixing. *Huthnance* [1981] described the high velocities in the vicinity of Bear Island. *Aagaard et al.* [1990] observed an unexpected behavior of tide amplitudes and velocities of the different tidal constituents. For example, at the Beaufort Sea shelf the sea level is dominated by the semidiurnal tide, and in contrast, the flow is usually dominated by the diurnal tide. *McPhee* [1991] and *Muench et al.* [1992] demonstrated that the tidal flow

maintains the unusually thick mixed surface layer over the Yermak Plateau and increases the vertical exchange of heat between the Atlantic water and the ocean surface. Recent measurements and tidal current analysis over the Yermak Plateau have been summarized by *Padman et al.* [1992]. Their measurements clearly show that Atlantic layer mixing is enhanced by tidally generated wave packets.

The general knowledge of the diurnal tides in the Arctic Ocean is due both to coastal observations and numerical models. A realistic picture of the Arctic diurnal tides was obtained through numerical modeling by *Schwiderski* [1981a, b], *Gjevik and Straume* [1989] and *Proshutinsky* [1991]. There are four available sources of information on spatial structure of the diurnal tides in the Arctic Ocean. *Defant* [1924] developed a one-dimensional hydrodynamical model, solved it by the finite difference method, and obtained the spatial distribution of diurnal tides in the Arctic Ocean. *Sterneck* [1928] used both observations and the simple model. In the charts constructed through the Defant and Sterneck studies, the diurnal tide in the Arctic Ocean had the form of progressive wave with one amphidrome at the southern edge of Spitsbergen. Their most important conclusion was that the diurnal tides in the Arctic Ocean, in contrast to semidiurnal tides, are caused almost entirely through the influence of astronomical forcing. The realistic charts for the diurnal waves were constructed by *Schwiderski* [1981a, b]. He used a detailed hydrodynamical interpolation model and included all available sea level observations as boundary conditions. Therefore his results are close to the obser-

¹Now at Institute of Marine Science, University of Alaska, Fairbanks.

Copyright 1993 by the American Geophysical Union.

Paper number 93JC01363.
0148-0227/93/93JC-01363\$05.00

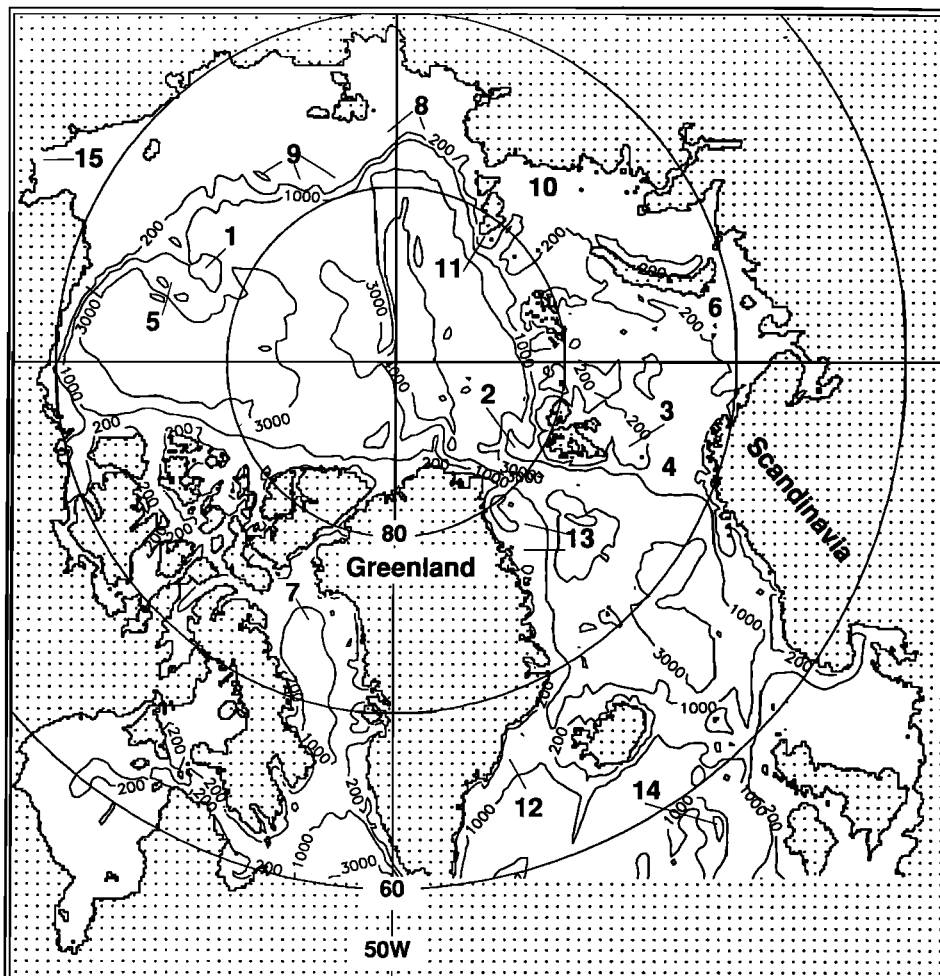
vations, especially in the coastal regions. But his model had a rather low resolution of 1° and could not resolve all features of the tidal waves in Arctic regions.

Tidal charts with improved resolution for the K_1 wave were obtained by *Gjevik and Straume* [1989] and *Proshutinsky* [1991] using local models of the Arctic Ocean with a spatial resolution of about 50 km. In contrast with the *Schwiderski* [1981a] result, two well-developed and connected amphidromes occurred east of Bear Island and between Bear Island and Spitsbergen. The O_1 tidal charts in the Arctic Ocean published by *Proshutinsky* [1991] with a spatial resolution of 50 km revealed the detailed structure of the amphidromic points in the vicinity of the Canadian Archipelago and in the Laptev and East Siberian Seas. An interesting result was obtained in the region of the Chukchi Cap. The O_1 wave propagated over this region in about 0.5 hour, while the travel time for the K_1 tidal wave was several hours. There was no explanation for this phenomenon.

These models used rather low spatial resolution and

therefore were unable to resolve mesoscale tidal patterns related to shelf waves. Nonetheless thorough analysis of the results obtained by *Gjevik and Straume* [1989] and *Proshutinsky* [1991] shows maxima in the sea level which were caused by the local topographic modification of the diurnal tides. In this paper we construct a numerical model with a resolution of about 14 km to study diurnal tidal constituents in the Arctic Ocean.

The model domain includes the Arctic Ocean, all the Nordic Seas, Hudson Bay, and Baffin Bay. The information on tidal constituents from more than 200 tide stations is used for comparison against the numerical results. The numerical domain and the bathymetry have been depicted in Figure 1. The purpose of the work is to use a high-resolution model to study the distribution of sea level and currents in the diurnal tidal range and to delineate the regions of near-resonant interaction of the tide with bottom topography. First, we model the observed current enhancement in the Yermak Plateau area, and afterwards we search for similar properties in the various regions of the Arctic Ocean



1 - Chukchi Cap; 2 - Yermak Plateau; 3 - Spitsbergenbanken; 4 - Barents-Norwegian Seas shelf; 5 - Arlis Plateau; 6 - Gusinaya Bank; 7 - Baffin Bay; 8 - Laptev Sea shelf edge; 9 - East-Siberian shelf edge; 10 - Kara Sea; 11- Severnaya Zemlia shelf edge; 12 - South Greenland Atlantic shelf edge; 13 - Greenland Sea shelf; 14 - Rockal Bank edge; 15 - Bering Strait

Fig. 1. Computational domain. Numbers denote major bathymetric features.

(Chukchi Cap, Arlis Plateau, the shelf area in the vicinity of the New Siberian Islands, and so on). The paper is organized in the following manner. Basic equations and boundary conditions are described in section 2. The data base is discussed in section 3; the model results are given in section 4; and the summary and discussion are in section 5.

2. BASIC EQUATIONS AND BOUNDARY CONDITIONS

We shall use a system of equations of motion and continuity written in vector notation and in the stereographic polar coordinate system [Kowalik and Bich Hung, 1977; Gjevik and Straume, 1989]:

$$\frac{d\mathbf{U}}{dt} + f\mathbf{k} \times \mathbf{U} = -gm\nabla(\alpha\zeta - \beta\zeta_0) + N_h m^2 \nabla^2 \mathbf{U} - \frac{r}{\rho D^2} \mathbf{U} |\mathbf{U}| \quad (1)$$

$$\frac{\partial \zeta}{\partial t} = -m^2 \nabla(\mathbf{U}/m) \quad (2)$$

Here, x, y are lateral coordinates, with their origin at the North Pole; t is time; ζ denotes free surface elevation; \mathbf{U} is volume transport with components along x and y directions; ρ denotes water density; N_h is horizontal eddy viscosity ($=5 \times 10^7 \text{ cm}^2/\text{s}$); D is total depth ($= H + \zeta$); H is equilibrium depth; f denotes Coriolis parameter; g is gravity acceleration; r is bottom friction coefficient ($=2.6 \times 10^{-3}$); ζ_0 denotes equilibrium tide; α, β are parameters accounting for tidal potential perturbations; \mathbf{k} is unit vector along vertical direction and m denotes map coefficient.

The stereographic polar coordinate system used in (1) and (2) is very close to the rectangular system of coordinates. The difference is due to the map coefficient m . It describes map correction from spherical projection to polar stereographic projection; its value changes from 1.000 at 90°N to 1.071 at 60°N . In our computations we have chosen the x and y axes of the stereographic system to be directed along 40°E and 130°E .

Only two tidal constituents, namely, K_1 and O_1 , are included in the computations. The generation of the K_1 and O_1 constituents is done through the open boundaries of the computational domain and through the astronomical forcing given in (1).

The tidal forcing is described in (1) through the terms which are multiplied by coefficients α and β . These terms include the tide-generating potential, but they also contain various corrections due to Earth tide and ocean loading [e.g., Schwiderski, 1981a, b]. Coefficient α defines the ocean loading and self-attraction of the ocean tides. Its value ranges from 0.940 to 0.953 according to Ray and Sanchez [1989]. The higher order correction for the loading effect can be implemented as well [e.g., Francis and Mazzega, 1990]. The term $\beta\zeta_0$ includes both the tide-generating potential and the cor-

rection due to the Earth's tide. It is usually expressed as

$$\beta\zeta_0 = (1 + k - h)\zeta_0 \quad (3)$$

Here k and h denote Love numbers, which are equal to 0.302 and 0.602, respectively. These numbers are averaged over all tidal constituents. The values for the individual constituent may differ and, according to Wahr [1981], for the K_1 constituent $k = 0.256$ and $h = 0.520$; thus $\beta = 0.736$.

The equilibrium tide for the diurnal constituents is

$$\zeta_0 = H_n \sin 2\phi \cos(\sigma_n t + \lambda) \quad (4)$$

Here $H_n = 14.565 \text{ cm}$, $\sigma_n = 0.729221 \times 10^{-4} \text{ s}^{-1}$ for K_1 , and $H_n = 10.051 \text{ cm}$, $\sigma_n = 0.675981 \times 10^{-4} \text{ s}^{-1}$ for O_1 ; λ denotes latitude angle.

To obtain a unique solution to the above system in the domain of integration, it is sufficient to specify normal and tangential volume transport everywhere along the boundaries [Marchuk and Kagan, 1977].

Initially, the dependent variables in the integration domain are taken as zero:

$$\zeta(x, y)_{t=0} = 0 \quad (5)$$

$$\mathbf{U}(x, y)_{t=0} = 0 \quad (6)$$

Along the solid boundary (S), we assume a no-slip condition for the volume transport

$$\mathbf{U}(x, y, t)_S = 0 \quad (7)$$

On the open boundary (O) of the domain, often only the sea level is known. In such cases, according to Marchuk and Kagan [1977], a unique solution cannot be obtained to (1) and (2). Therefore we proceed as follows: in the vicinity of the open boundary (along the first line parallel to the open boundary), the linear hyperbolic problem is solved (horizontal friction and advective terms in (1) are neglected). This procedure yields a unique solution for the volume transport with sea level defined at the open boundary [e.g., Rammung and Kowalik, 1980]. When the volume transport is specified along the line parallel to the open boundary the solution process for the full set of equations (parabolic problem) can be extended into the integration domain. With the above restriction the boundary conditions pertinent to equations (1) and (2) can be stated as follows:

$$\mathbf{U}(x, y, t)_O = 0 \quad (8)$$

$$\zeta_O = \zeta(x, y, t) \quad (9)$$

We also stipulate conservation of mass in the integration domain by taking the integral over one tidal period (T) along the entire open boundary (O) of the integration domain:

$$\int_0^T \int_O U_n dt dO = 0 \quad (10)$$

Here U_n is volume transport component directed normal to the open boundary.

A no-slip condition along the solid boundary on the staggered C (Arakawa) grid is easily implemented as no flow. Along the open boundaries, amplitudes and phases for every tidal constituent are specified. This is done from the model results obtained by Schwiderski [1981a, b] and Zahel [1973], satellite observations [Cartwright *et al.*, 1991], and from coastal tide stations.

In the ensuing computations, one additional simplification is introduced. Because the Arctic Ocean is covered by mobile pack ice and its effect on the tides is usually small [e.g., Kowalik, 1981], the influence of the pack ice is neglected.

3. DATA BASE

To cover the Arctic Ocean with a 14-km spatial grid step required a thorough examination of the data base on depth distribution. Quite recently, Weber and Sweeney [1985, p. 664] wrote of a major bottom feature in the Arctic Ocean: "Lomonosov Ridge is up to 34 km farther south than is shown on the latest international map." We hoped that the depth data for the model could simply be taken from the data base ETOPO5 released by the National Geophysical Data Center. This proved to be a wrong assumption. The comparison of ETOPO5 data and Russian and Norwegian charts has shown major differences. In the Beaufort Sea these differences reach 2000 m [Glavnoe Upravlenie po Navigacii i Okeanografii, 1985] and the depth was corrected according to the Russian data. In the Barents Sea and the Kara Sea the depth was compiled from the Norwegian [Norsk Polarinstitutt, 1989] and U.S. charts [Geophysical Society of America, 1991]. Large-scale bottom features in the Greenland, Laptev, and Beaufort Seas were compiled from *Naval Research Laboratory*, [1986]. As it will be shown, these corrections have an important role in tidal dynamics of the Arctic Ocean.

The model results were verified through comparison with observation. Two kinds of observations are available to perform this comparison.

1. The sea level observations are available from more than 200 sites around the Arctic Ocean. These are mainly data from tide gauges located at the shore, while some data are from the shelf area (pelagic stations). No data are available from the deep ocean. A series of about 3 years of pressure data was recorded at the 568 m depth close to Spitsbergen [Morison, 1991]. This is probably the farthest north recorded sea level data. The principal source for the pelagic tidal constants is an International Association for Physical Sciences of the Oceans publication by Cartwright and Zetler [1985]. The tidal constituents information for the tide gauges located at the shore were taken from *Gidrographicheskoe Upravlenie VMF SSSR* [1941] and *Hydrographer of the Navy* [1987]. Some tide data we received from the Canadian Hydrographic Service and the International Hydrographic Bureau in Monaco.

2. Current meter data from 14 locations are available for comparison against the model results. Most measurements were taken in the Norwegian, Barents, and Beaufort Seas. The current meter data were published by Aagaard *et al.* [1985], Aagaard *et al.* [1990], Huggett *et al.* [1975], and Huthnance [1981].

As a third source of information, we use the results from the Schwiderski [1981a, b] model. A comparison against Schwiderski's model is made at more than 6000 grid points. The purpose of this comparison is to locate differences between the low-resolution Schwiderski model (1^0 space grid) and the high-resolution model with about a 14-km space grid.

4. RESULTS

The diurnal tide wave simulations have been carried out with different versions of the model in order to assess the effects of the tide-generating forces, horizontal eddy viscosity, bottom friction, and nonlinear terms. The integration in time for each component (K_1 and O_1) was done separately and usually proceeded for 20 tidal periods until a stationary distribution of total energy occurred. To compensate for the possible interaction between dominant tidal constituent M_2 and diurnal tides, which may lead to damping of the diurnal tides, we have slightly increased the horizontal eddy viscosity. After a series of experiments we have arrived at a value of $5 \times 10^7 \text{ cm}^2 \text{ s}^{-1}$ for the horizontal eddy viscosity.

The diurnal tide generation is accomplished both by astronomical forcing and boundary conditions. The astronomical forcing is well defined in (1), but the boundary conditions ought to be interpolated from available data to the 14-km numerical grid we are using. At the southern boundary the amplitudes and phases of K_1 and O_1 are taken from Schwiderski's [1981a, b] numerical grid of 1^0 distance and from Cartwright *et al.* [1991]. The missing values for our numerical grid are linearly interpolated from these data. In the Bering Strait the open boundary conditions are interpolated from the data recorded at three tide stations. This procedure proved to be satisfactory in establishing the required open boundary conditions.

The tidal charts of K_1 and O_1 diurnal waves are shown in Figures 2a and 2b and Figures 3a and 3b, respectively. Principal axes of the K_1 and O_1 tidal current ellipses are given in Figures 4a, 4b, 4c and 4d and in Figures 5a, 5b, 5c and 5d, respectively.

4.1. Structure of the Cotidal, Corange, and Tidal Ellipses Charts

The numbers on the corange lines in Figures 2a and 3a are given in centimeters. Phase angle on the cotidal charts in Figures 2b and 3b is referred to Greenwich and is expressed in degrees. The ellipse charts have been divided into four regions because of highly differentiated tidal current magnitude in these regions.

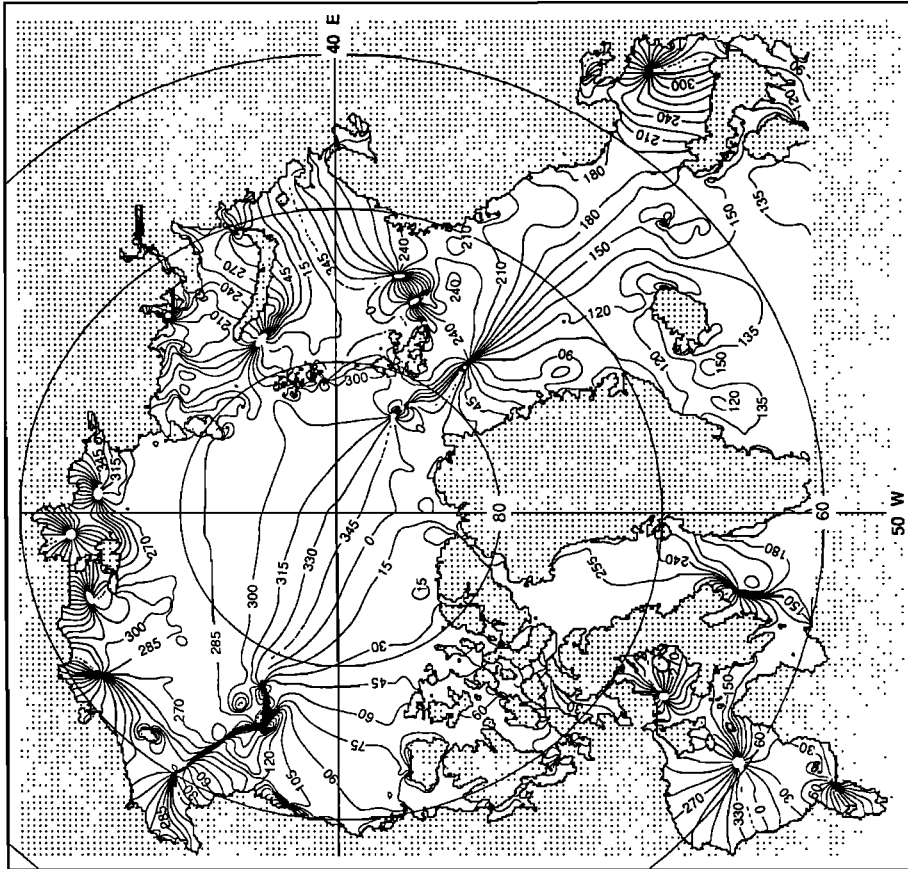


Fig. 2b. Computed phase (in degrees) of surface elevation for the diurnal constituent K_1 .

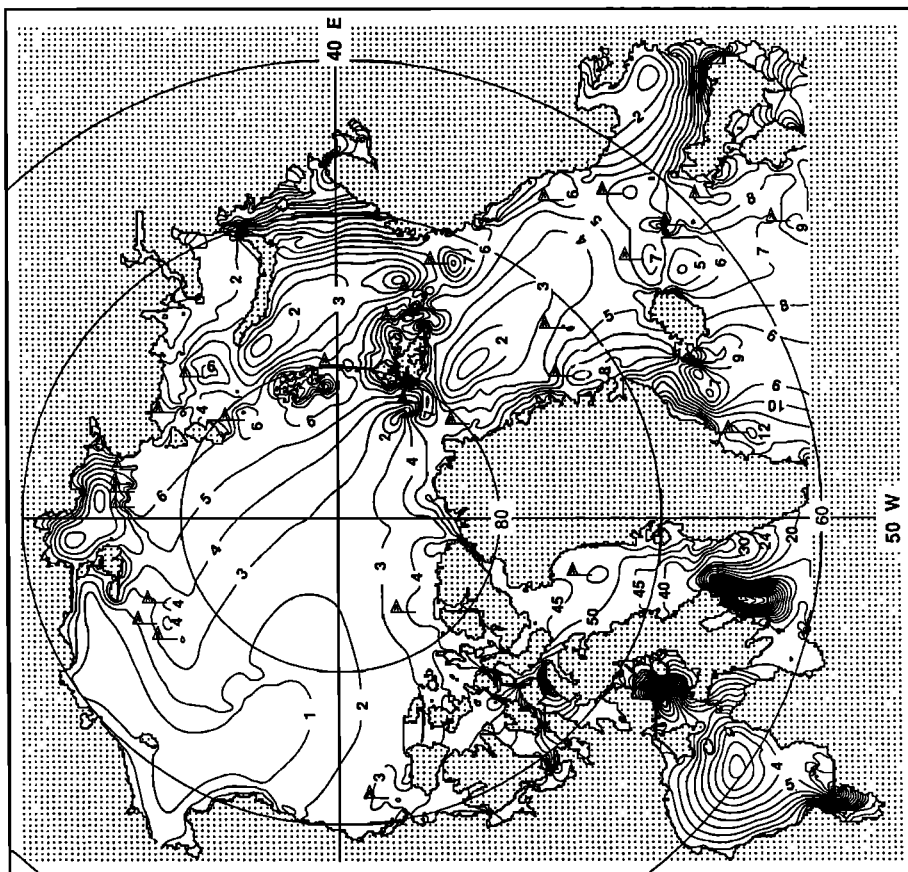


Fig. 2a. Computed amplitude (in centimeters) of surface elevation for the diurnal constituent K_1 . Flags denote shelf wave regions.

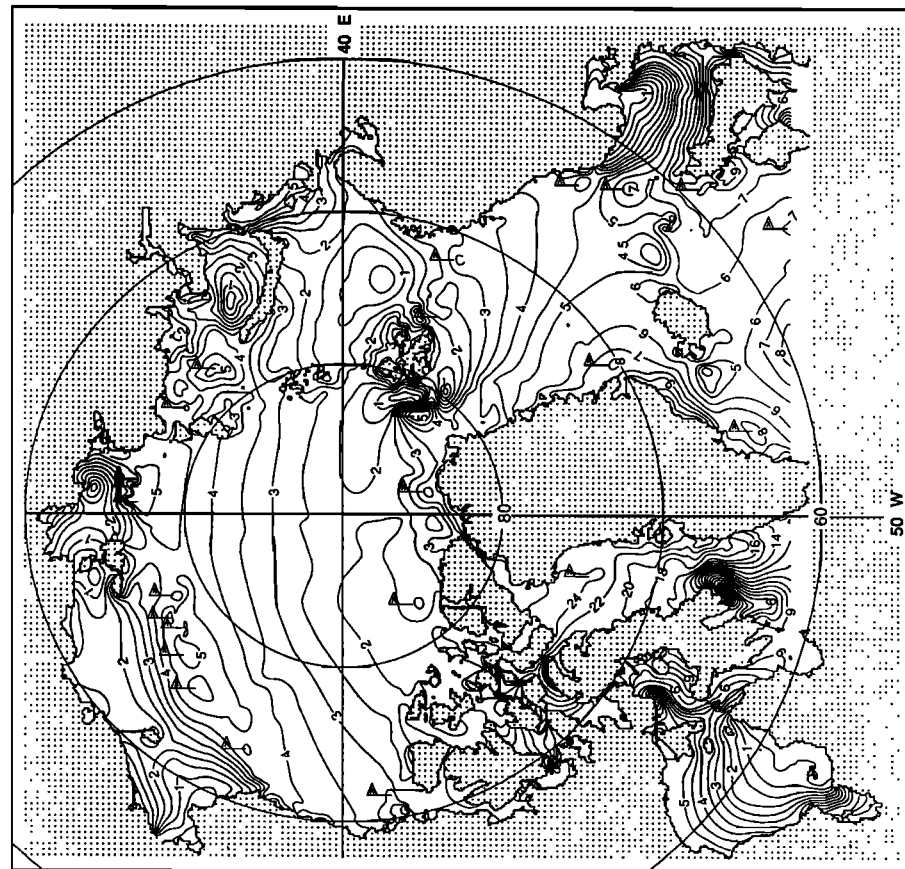


Fig. 3a. Computed amplitude (in centimeters) of surface elevation for the diurnal constituent O_1 . Flags denote shelf wave regions.

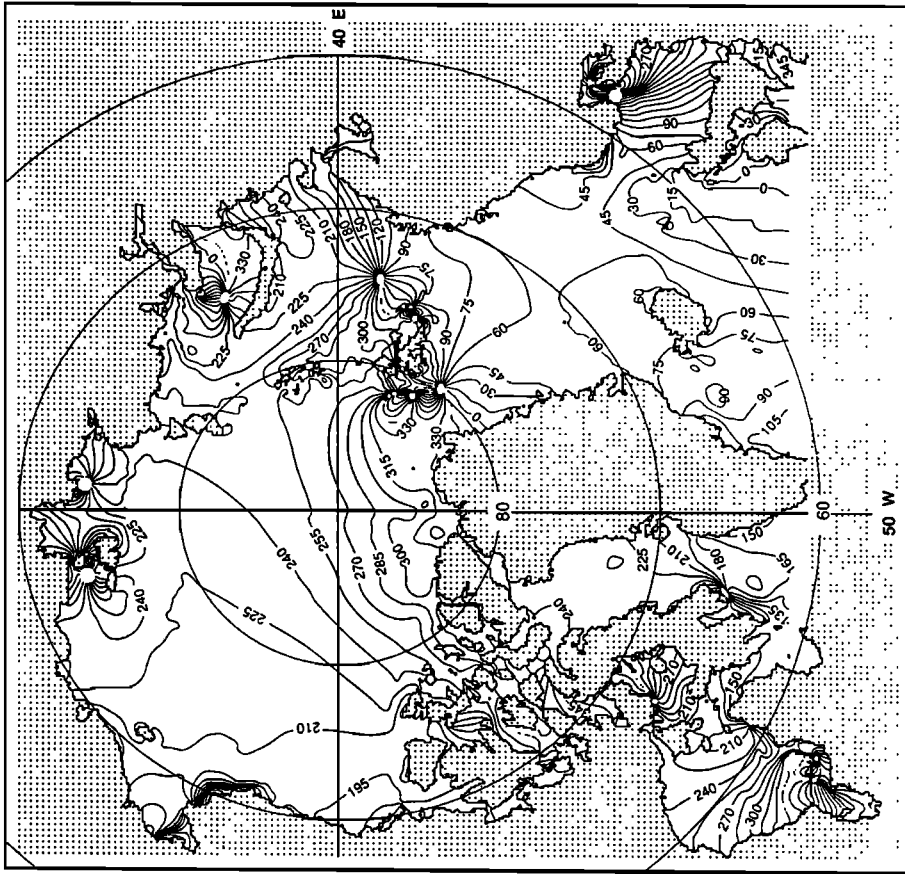


Fig. 3b. Computed phase (in degrees) of surface elevation for the diurnal constituent O_1 .

The K_1 and O_1 tidal charts computed with a 14-km space grid possess an unexpected pattern in many locations, that differs from the "classical" charts obtained previously. The homogeneous structure of the classical tidal pattern is often broken by local regions of increased amplitude often associated with the local system of cotidal lines (Figures 2a, 2b, 3a, and 3b). In the same regions the enhanced tidal currents occur as shown in Figures 4 and 5. We have also noted that these regions of variable amplitude and phase are often confined to the shelf edge of a nonuniform bottom topography. We believe that this shorter wavelength phenomenon occurs at the seamounts, submarine peninsulas and bays. We shall shortly describe this phenomenon in two regions: the Yermak Plateau and the Chukchi Cap.

In the Arctic Ocean the new K_1 chart is somewhat similar to the chart obtained previously by *Schwiderski* [1981a], *Gjevik and Straume* [1989] and *Proshutinsky* [1991]. The main amphidrome (Figure 2b) at the entrance to the Arctic Ocean for the K_1 wave is still located in the Fram Strait, but it is connected with a small twin amphidrome system in the vicinity of the Yermak Plateau. These amphidromic points are located at $\lambda=10^{\circ}48'E$, $\phi=82^{\circ}36'N$ and $\lambda=10^{\circ}18'E$, $\phi=82^{\circ}00'N$, i.e., at a distance of about 60 km. Close to the twin amphidrome, a dome of increased sea level with a maximum of about 8 cm is formed (an anti-amphidromic point). Fortunately, the existence of the increased sea level can be confirmed by *Morison's* [1991] measurements taken at the southeastern flank of the dome (observed amplitude is 6.9 cm and phase is 233° for the K_1 constituent at $\lambda=8^{\circ}07'E$, $\phi=79^{\circ}52'N$). At the same location, *Schwiderski's* computations produced 3 cm for the amplitude and 251° for the phase, and from our computations the values are 6.9 cm and 260° . The currents for the K_1 wave in the Yermak Plateau region (Figure 4b) also display strong enhancement. This confirms the observations by *Hunkins* [1986] and *Padman et al.* [1992]. In the ensuing considerations, it will be shown that this behavior is a result of the near-resonant diurnal wave interaction with the Yermak Plateau topography because the resonance peak related to the natural oscillations of the Yermak Plateau is close to the diurnal band (Table 3).

The main amphidrome system in the Central Arctic Basin has changed its position. It is located close to the Chukchi Cap, forming a very complicated cotidal and corange structure with twin amphidromic points. This twin system is located at $\lambda=166^{\circ}36'W$, $\phi=73^{\circ}30'N$ and $\lambda=159^{\circ}48'W$, $\phi=75^{\circ}18'N$. The distance between the points is about 300 km. The twin system is connected with the main amphidromic point in the Chukchi Sea, located at $\lambda=171^{\circ}24'W$, $\phi=70^{\circ}6'N$. Across the connecting line, travel time for the K_1 wave is very long (about 3 hours), which indicates that this is an amphidromic line (Figure 2b).

The structure of the O_1 wave given in Figures 3a and 3b is close to the K_1 wave, but the position and

number of the amphidromic points are different. First of all, the period of these diurnal waves differ about 1.88 hours. This difference caused a change in the interaction with the bottom topography. In the K_1 wave the strongest flow occurred at the shallow Spisbergenbanken (Figure 4b), but in the O_1 wave the largest flow was at the Yermak Plateau (Figure 5b). This indicates a stronger interaction of the O_1 wave with the Yermak Plateau topography. Such behavior is easily explained by the fact that the period of natural oscillations for the Yermak Plateau (25.6 hours) is much closer to the O_1 wave than to the K_1 wave (Table 3).

The set of amphidromic points in the vicinity of the Yermak Plateau is similar to the K_1 wave, but the position of the O_1 amphidromes is rotated about 45° around the Yermak Plateau and the region of maximum amplitude of the sea level elevation (anti-amphidromic point) is moved to the north of the Yermak Plateau (Figure 3a).

The main O_1 amphidrome located in the previous charts in the Central Arctic Basin is now located in the passages of the Canadian Archipelago.

We also note very weak interaction of O_1 with the bottom topography over the Chukchi Cap. The O_1 wave travels over this region in about 0.5 hour (Figure 3b).

4.2. Comparison Against Observed Sea Level Data

Modeling accuracy is estimated by comparison against 187 coastal and 24 pelagic stations (some stations from the available data base are not included in the comparison because they are located in the small bays and rivers not resolved by the 14-km grid step). In Table 1 the mean absolute errors between observed and computed amplitudes for O_1 and K_1 waves are given. To demonstrate the proximity of calculated and measured amplitudes, we use coefficient, intercept, and standard deviation of the linear regression line. The coefficients of correlation between two sets of data are calculated as well. The best agreement is obtained for the coastal stations with a coefficient of correlation equal to 0.967 for the K_1 wave and 0.952 for the O_1 wave. Very good agreement is achieved for the pelagic stations located in the North Atlantic. Here correlation coefficients are 0.962 and 0.951 for K_1 and O_1 waves, respectively.

One can see that the computed amplitudes for the entire integration domain, both for the K_1 and O_1 waves, are higher than the measured amplitudes with a mean difference of 1.00 cm (K_1) and 0.41 cm (O_1) for the pelagic stations and 0.10 cm (K_1) and 0.37 cm (O_1) for the coastal stations.

Comparison against *Schwiderski's* [1981a, b] computations shows the smallest correlation coefficients: 0.945 and 0.935. Although his computations, by definition, included all tidal data from the coastal stations, the main difference is due to the calculated amplitude in the open ocean. Due to the spatial grid used by *Schwiderski*, many details of the bottom topography

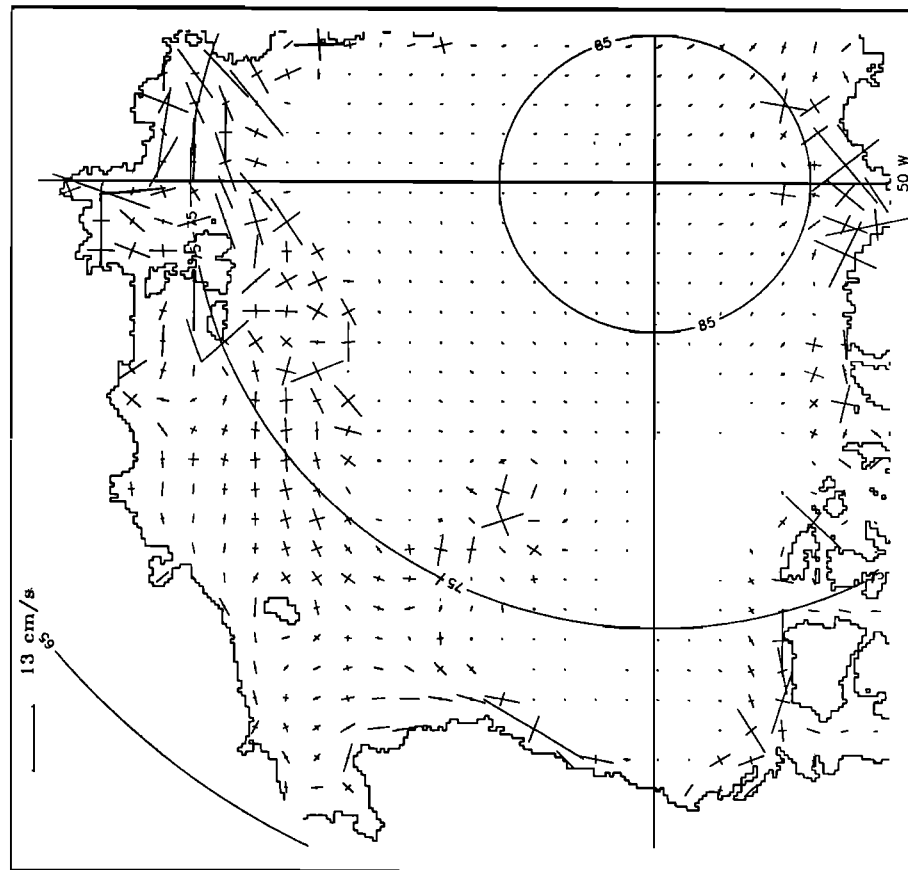


Fig. 4a. Principal axes of the K_1 tidal current ellipses in the Arctic Ocean (part 1).

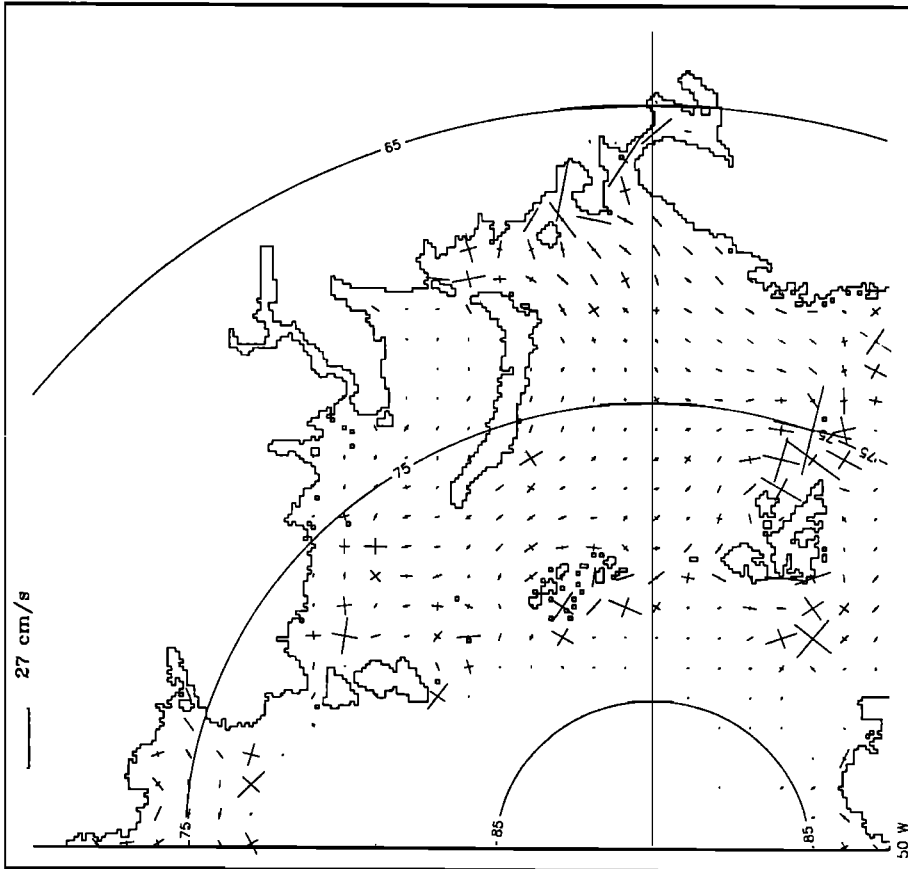


Fig. 4b. Principal axes of the K_1 tidal current ellipses in the Arctic Ocean (part 2).

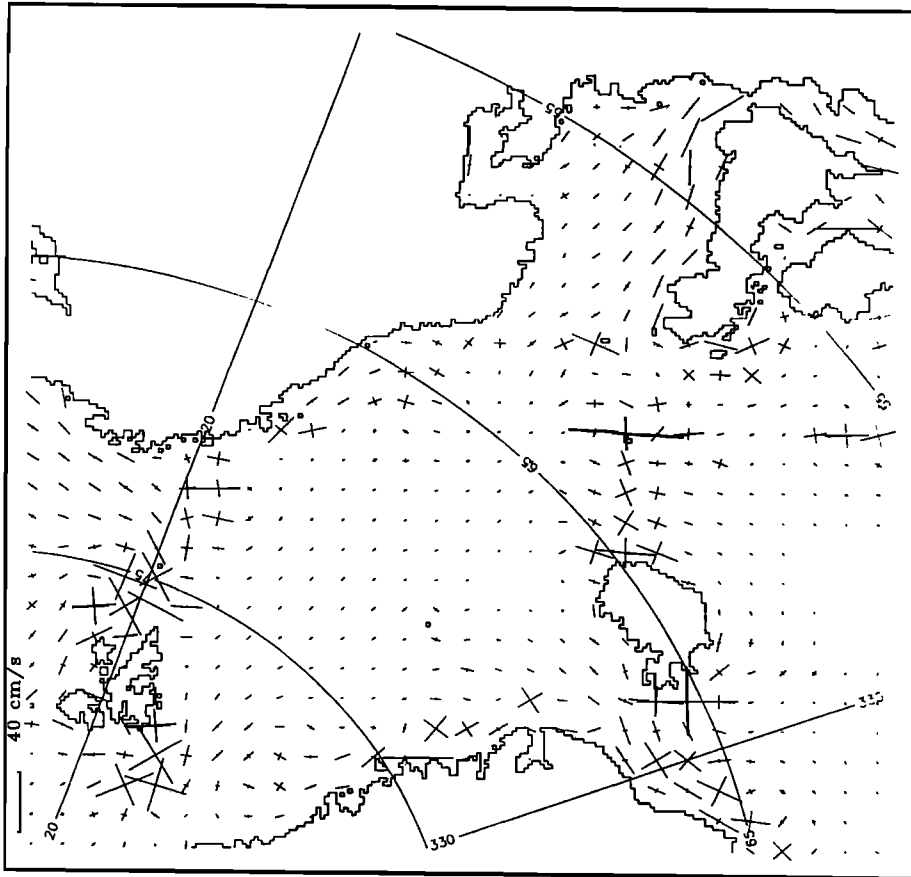


Fig. 4d. Principal axes of the K_1 tidal current ellipses in the Norwegian and Greenland Seas and North Atlantic Ocean.

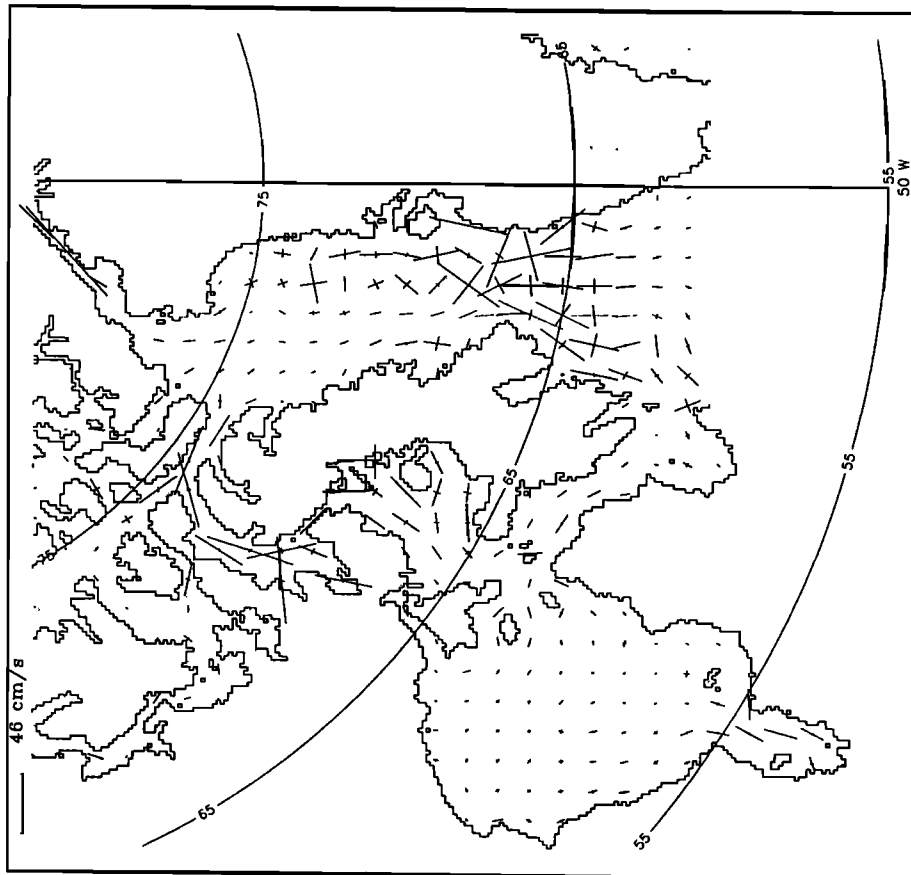


Fig. 4c. Principal axes of the K_1 tidal current ellipses in Hudson Bay and Baffin Bay.

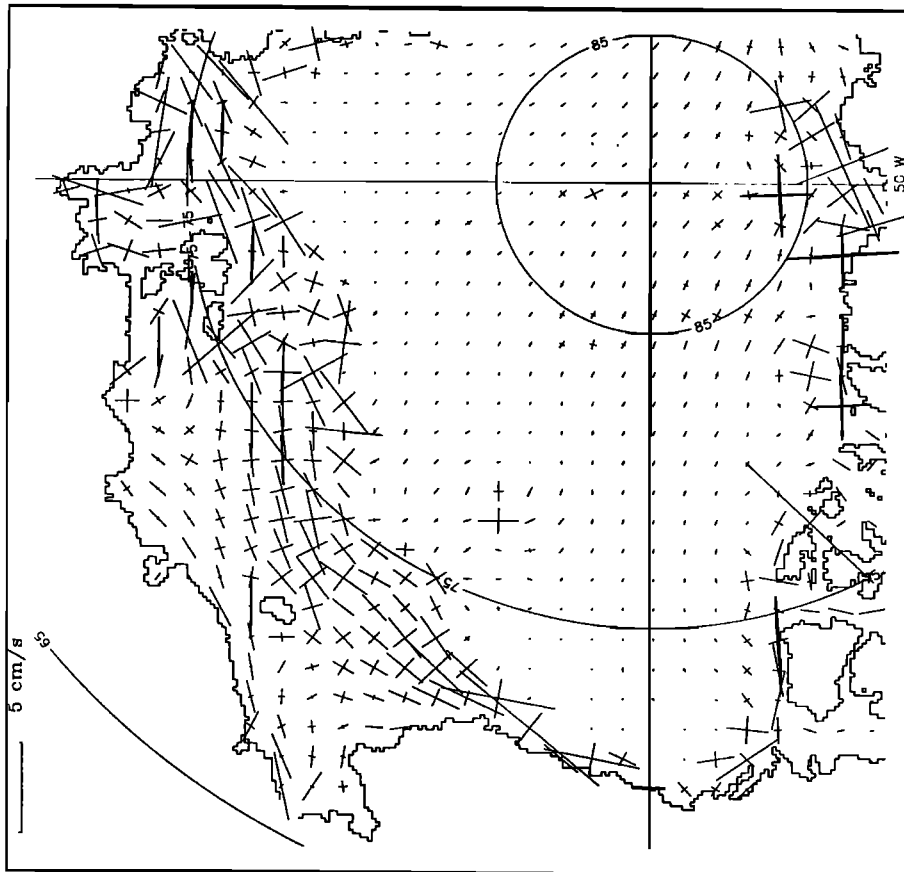


Fig. 5a. Principal axes of the O_1 tidal current ellipses in the Arctic Ocean (part 1).

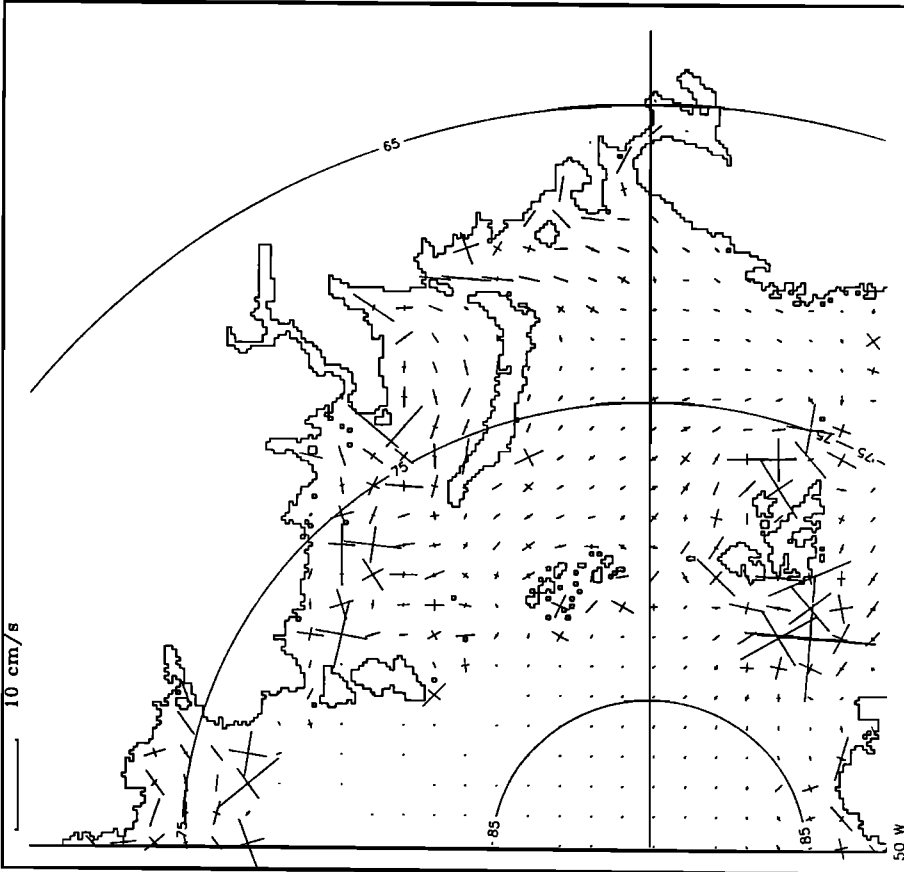


Fig. 5b. Principal axes of the O_1 tidal current ellipses in the Arctic Ocean (part 2).

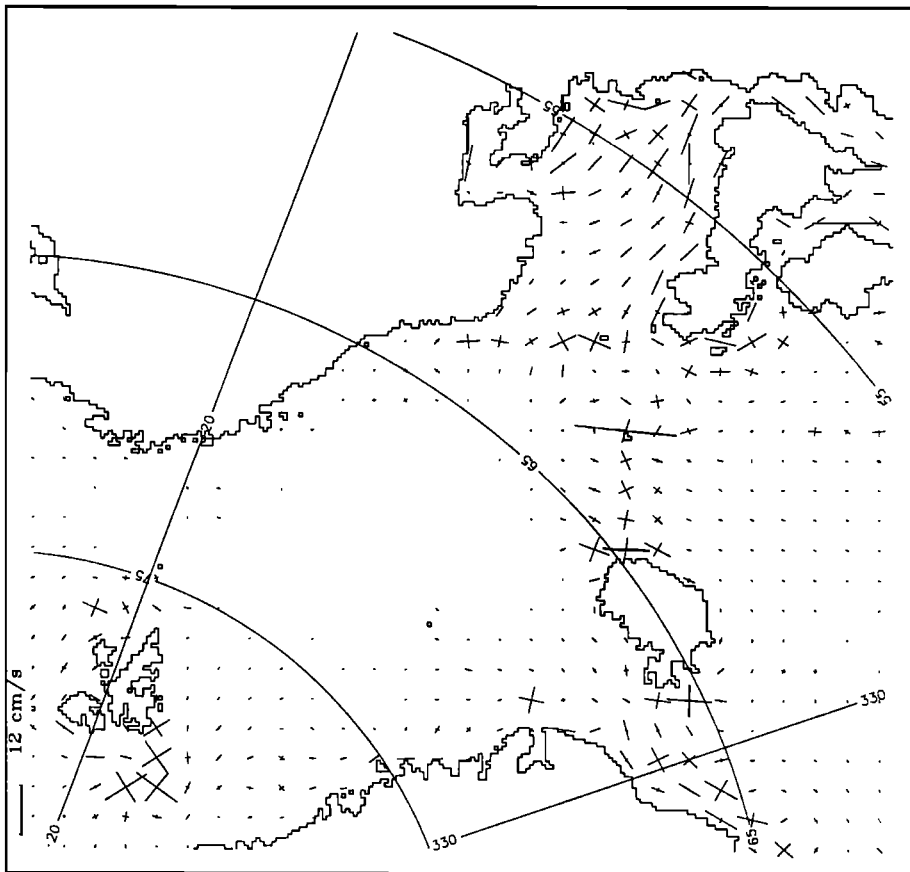


Fig. 5d. Principal axes of the O_1 tidal current ellipses in the Norwegian and Greenland Seas and North Atlantic Ocean.

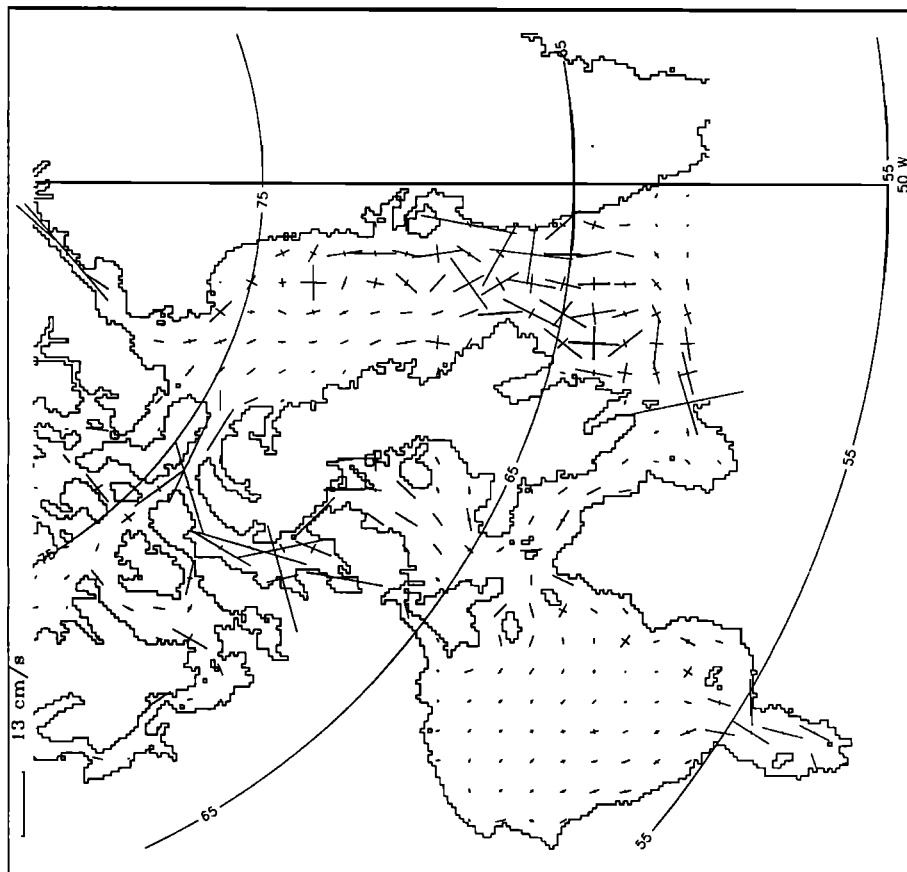


Fig. 5c. Principal axes of the O_1 tidal current ellipses in Hudson Bay and Baffin Bay.

TABLE 1. Mean Absolute Error (*MAE*), Intercept (*I*), Coefficient (*B*), Standard Deviation (*S*) of a Linear Regression Line, and Correlation Coefficient (*R*) Between Observed and Computed Amplitudes of K_1/O_1 Waves

Data Base	<i>MAE</i> , cm	<i>I</i> , cm	<i>B</i>	<i>S</i> , cm	<i>R</i>
Coastal stations (187)	1.40 0.92	0.10 0.37	0.99 0.91	±1.89 ±1.04	0.967 0.952
Pelagic stations (24)	1.42 0.78	1.00 0.41	0.98 0.90	±1.91 ±1.11	0.962 0.951
Schwiderski's model	1.72 0.81	1.29 0.70	0.97 0.85	±2.08 ±1.32	0.945 0.935

were smoothed. The regions of the shelf waves of tidal origin were not resolved. These reasons generated differences between the two models which resulted in the low correlation coefficients.

The calculations turned out to be closest to the observations along the Scandinavian coast, the southern part of the Barents Sea (including the entrance to the White Sea where observed amplitude is 8.0 cm and computed is 8.1 cm), and on the islands in the Norwegian, Greenland, and Barents Seas. Very good results are obtained in the vicinity of Spitsbergen and Franz Josef Land. For the 14 stations on the coast of Spitsbergen the mean absolute error in tidal amplitude is 0.6 cm and the mean absolute phase error is 15° . A significant result is obtained for the open sea level in the vicinity of Yermak Plateau. Here *Morison's* [1991] observation and our calculations of the K_1 amplitude (6.9 cm) are identical. This confirms the existence of the elevated sea level in close proximity to the regions of enhanced currents.

Data from three stations on Franz Josef Land are available. The mean absolute errors of amplitude and phase are 0.2 cm and 12° , respectively. The computed and observed data are in good agreement for the eastern part of the Kara Sea, where phase error does not exceed 9° and the average amplitude error equals 0.5 cm. For the southern Kara Sea, however, the computed amplitudes are 20% lower than observed. Relatively larger errors occur in the northern part of the Baffin Bay, where computed amplitudes of K_1 and O_1 are approximately 25% higher than observed. Also, larger errors are found in the narrow passages of the Canadian Archipelago. These errors are due to both the scant bathymetric data (in some regions we still use ETOPO5) and scant tidal data.

Harmonic constants in the Arctic Ocean tides are unstable, having seasonal variations due to the changing ice cover [*Fjeldstad*, 1936; *Dvorkin*, 1970; *Murty*, 1985]. For a number of stations on the Arctic coast the variability of the harmonic constants is comparable to the modeling errors. We must also stress that the observational data also have errors since the harmonic analysis is mostly based on the short-term observational series taken during the summer and autumn periods. In many regions of the Arctic Ocean during these seasons, the tidal sea level variations are small compared

to sea level oscillations caused by storm surges [*Fjeldstad*, 1936; *Kowalik*, 1984].

The results of numerical experiments showed that the differences in approximating ocean depths, coastlines and conditions at the open boundary are primary sources of the errors in calculated tidal amplitude, rather than other factors in the model equations.

4.3. Comparison Against Current Data

Principal axes of the K_1 and O_1 tidal current ellipses are shown in Figures 4 and 5, respectively. The major regions of current enhancement are clearly delineated in these charts. The current meter data base in the diurnal tidal band is very scant in the Arctic Ocean. The comparison of computed currents against observed currents given in Table 2 is therefore very limited and is done only for the K_1 component.

In Table 2 the observed and calculated K_1 tidal currents are described by the parameters of the tidal ellipse: major half-axis (*A*), minor half-axis (*B*), azimuth angle of the major axis, and the direction of rotation. The azimuth angle is positive clockwise from the North direction and negative counterclockwise. At the Scandinavian Shelf and Barents Sea the calculated currents turned out to be in satisfactory agreement with those obtained from observations. It is interesting to note that *Huthnance* [1981] observed strong current enhancement of the K_1 wave at the point $\phi = 71^\circ 30'N$, $\lambda = 19^\circ 00'E$. Our calculations agree well with this measurement but they also show that the largest currents of about 34 cm s^{-1} are located beyond this area at the Spitsbergenbanken (Table 3).

One region which has a relatively better data base is the shelf of the Beaufort Sea. The measurements of *Aagaard et al.* [1990] at the western flank and *Huggett et al.* [1975] on the eastern flank allow comparison with the model and depict the tidal current pattern over the entire shelf. *Aagaard et al.* [1990] observed that the tidal currents in the western Beaufort Sea were small, typically 5 cm s^{-1} or less, and a variance analysis showed that some 80% of the total tidal variance in the current record was in a diurnal band.

Huggett et al. [1975] recorded and analyzed tidal currents in the area from $\lambda = 138^\circ W$ to $\lambda = 128^\circ W$. The currents in this area were very small, of the order of

TABLE 2. Comparison of Observed (1) and Computed (2) K_1 Ellipse Parameters

Latitude	Longitude	Major Half-Axis A, cm s ⁻¹		Minor Half-Axis B, cm s ⁻¹		Azimuth Angle of A, degrees		Rotation (+ clockwise)	
		1	2	1	2	1	2	1	2
78° 59N	05° 15E	1.1	1.7	0.2	0.2	-37	-41	-	-
79° 00N	04° 25E	1.2	1.7	0.0	0.4	19	-13	-	-
78° 55N	03° 18E	1.4	1.8	0.1	0.4	-6	-11	-	-
65° 03N	07° 35E	2.4	2.0	1.6	1.4	104	61	+	+
66° 18N	09° 31E	2.4	1.8	1.4	0.7	41	32	+	+
66° 02N	07° 32E	1.6	1.7	0.9	0.9	58	50	+	+
71° 20N	25° 15E	2.6	2.4	0.7	0.5	80	94	+	+
71° 30N	19° 00E	2.8	3.4	2.1	2.7	-40	-25	+	+
72° 12N	19° 35E	2.3	2.3	1.3	1.4	-40	-31	+	+
72° 25N	23° 00E	1.7	1.7	0.7	0.3	-70	-70	+	+
73° 08N	21° 40E	2.5	2.2	0.5	0.6	-70	-74	-	-
73° 10N	19° 30E	2.0	2.3	0.0	0.1	-45	-45	-	-
73° 55N	19° 40E	15.5	14.4	9.0	9.1	-45	-35	+	+
74° 07N	19° 00E	18.6	19.4	12.5	14.9	-65	-55	+	+

TABLE 3. Predicted Regions and Parameters of Diurnal Shelf Waves

Latitude	Longitude	Maximum Velocity, cm s ⁻¹		Amplification Coefficient of Velocity		Sea Level Amplitude, cm		Natural Periods, hours
		K_1	O_1	K_1	O_1	K_1	O_1	
<i>West Beaufort Sea Shelf</i>								
71° 06N	128° 54W	6.0	3.9	3.0	3.5	4.0	3.3	25.0
<i>Arlis Plateau</i>								
75° 30N	179° 54E	-	1.4	-	2.0	-	5.2	25.6
<i>East Siberian Sea Shelf Edge</i>								
76° 48N	168° 48E	6.3	-	6.0	-	3.9	-	23.8
77° 18N	162° 06E	8.8	3.4	10.0	5.0	4.5	5.2	24.4
76° 36N	172° 24E	-	4.9	-	10.0	-	5.3	25.6
<i>Canadian Arctic Shelf Edge</i>								
82° 24N	99° 00W	1.7	1.5	5.0	5.0	4.5	2.6	25.0
83° 36N	69° 30W	8.4	3.2	10.0	8.0	5.7	3.4	24.4
<i>Baffin Bay</i>								
73° 12N	62° 54W	18.4	6.3	6.0	5.0	51.7	24.3	25.0
<i>Laptev Sea Shelf Edge</i>								
76° 42N	125° 42E	-	8.0	-	7.0	-	5.4	25.6
76° 42N	126° 12E	16.9	-	8.0	-	6.5	-	24.4
76° 54N	122° 18E	13.6	-	9.0	-	6.7	-	24.4
77° 06N	116° 36E	9.3	-	7.0	-	6.9	-	24.4
<i>Severnaya Zemlia Shelf Edge</i>								
80° 48N	80° 36E	9.4	2.7	9.0	8.0	7.0	2.7	25.6
<i>Kara Sea</i>								
78° 00N	94° 18E	13.0	3.3	10.0	8.0	6.2	5.2	25.6
80° 48N	80° 36E	9.4	-	9.0	-	7.0	-	24.4
81° 12N	77° 30E	14.8	-	12.3	-	7.0	-	24.4

TABLE 3. (continued)

Latitude	Longitude	Maximum Velocity, cm s^{-1}		Amplification Coefficient of Velocity		Sea Level Amplitude, cm		Natural Periods, hours
		K_1	O_1	K_1	O_1	K_1	O_1	
77° 24N	81° 00E	10.0	—	8.0	—	6.3	—	24.4
81° 18N	82° 42E	—	2.1	—	7.0	—	3.8	25.6
<i>South Greenland Atlantic Shelf Edge</i>								
63° 36N	37° 42W	8.4	5.3	6.0	5.5	14.4	8.7	25.0
<i>Yermak Plateau</i>								
80° 36N	03° 06E	14.8	—	12.0	—	8.1	—	25.6
81° 42N	04° 54E	—	13.2	—	18.0	—	5.8	25.6
<i>Greenland Sea Shelf</i>								
72° 06N	18° 24W	6.1	—	5.0	—	8.5	—	25.0
70° 00N	20° 00W	—	3.3	—	4.0	—	8.2	25.0
78° 42N	12° 36W	—	4.5	—	5.0	—	4.1	25.6
<i>Spitsbergenbanken</i>								
76° 00N	21° 12E	34.1	—	16.0	—	10.6	—	25.0
75° 42N	21° 06E	—	8.4	—	4.0	—	2.3	25.0
<i>Vicinity of Bear Island</i>								
74° 24N	18° 48E	27.8	—	10.0	—	7.3	—	23.8
74° 06N	19° 18E	—	8.7	—	8.0	—	2.8	23.8
<i>Barents Sea, Gusinaya Bank</i>								
71° 48N	47° 00E	8.7	—	5.0	—	8.5	—	24.4
<i>Barents-Norwegian Seas shelf Edge</i>								
71° 36N	17° 18E	9.9	2.7	8.5	5.0	10.1	3.7	25.0
<i>Faroe-Iceland Ridge North Edge</i>								
64° 12N	9° 00W	4.6	—	7.5	—	3.1	—	24.4
<i>Faroe-Iceland Ridge North Edge</i>								
64° 12N	9° 00W	4.6	—	7.5	—	3.1	—	24.4
<i>Faroe-Iceland Ridge South Edge</i>								
60° 36N	9° 12W	14.2	5.6	10.0	8.0	9.1	7.1	24.4
<i>Faroe-Shetland Trough East Edge</i>								
61° 54N	0° 00	3.1	—	3.0	—	7.2	—	25.0
<i>Faroe-Shetland Trough West Edge</i>								
61° 42N	7° 00W	—	2.4	—	10.0	—	7.5	25.6
<i>Rockall Bank</i>								
57° 30N	8° 12W	15.0	4.6	13.0	7.0	9.5	6.3	24.4
<i>Irland Trough Edge</i>								
56° 12N	16° 00W	7.8	—	7.0	—	9.5	—	25.6

0.5 cm s^{-1} , and towards the Amundsen Gulf velocity enhancement occurred to 1.2 cm s^{-1} .

Comparison against the model result is satisfactory with the maximum absolute error equal to 0.1 cm s^{-1} . Principal axes of the current ellipses in Figure 4a are in satisfactory agreement with the above pattern. Com-

puted currents depict slight enhancement to 5 cm s^{-1} in the vicinity of Barrow. At demarcation line between Canada and the United States, very small currents of the order of 1 cm s^{-1} occur. Again, currents are increasing in the vicinity to the Amundsen Gulf to 6 cm s^{-1} .

4.4. Shelf Waves of Tidal Origin

The K_1 and O_1 waves interact with nonuniform bathymetry along the continental slope, forming the short wave – shelf wave structure. Some parameters of these shelf waves are given in Table 3. More than 30 regions can be determined in the Arctic Ocean and North Atlantic Ocean with well-developed shelf waves. Here the maximum of calculated velocity is given for each location. The coefficient of velocity amplification defines the relation of the maximum velocity for the shelf wave to the average velocity calculated in the deep water surrounding the shelf wave region. The sea level amplitude in Table 3 denotes the maximum amplitude occurring at the anti-amphidromic points.

We also calculated the periods of natural oscillations in the velocity domain to find out how close the resonance periods are to the diurnal tidal waves. The method used to define the natural periods is similar to the method described by Platzman [1978]. The presence of major peaks in the velocity spectra with periods from 23.8 hours to 26.6 hours in each location, where the enhanced velocity is observed, proves that this phenomenon is caused by near-resonant interaction of the diurnal tidal waves with the bottom topography.

To elucidate further the process of shelf wave occurrence, we shall consider certain terms of the energy balance equation for the tidal waves. Crawford [1984] suggested using the energy flux to observe generation and dissipation of the shelf wave of tidal origin. The components of the energy flux vector E_h along the x and y directions are

$$E_h = \{ \rho u D[(u^2 + v^2)/2 + g\zeta], \\ \rho v D[(u^2 + v^2)/2 + g\zeta] \} \quad (11)$$

Here u and v are the components of the vertically averaged velocity.

We shall use the first-order approximation to the above definition (not valid in very shallow water)

$$E_h = \{ \rho g H u \zeta, \quad \rho g H v \zeta \} \quad (12)$$

Tide waves propagating in an oceanic basin are the superposition of traveling and standing waves. Energy flux due to the standing wave when averaged over the tide period is equal to zero; only a traveling wave transports energy. The flux of energy will also change in the regions of generation and dissipation of tidal energy.

The average energy flux over a tidal period for the K_1 and O_1 waves is shown in Figures 6 and 7. There are two sources of tidal energy in the diurnal band. The main source of energy, located in the central Arctic Ocean, is due to astronomical forcing. The second source of energy is an advective flux from the Atlantic Ocean. In the pattern of the energy flux one can see regions of clockwise and counterclockwise rotation. Rotation around amphidromic points is counterclockwise. The rotation around an anti-amphidromic point is clock-

wise; this is the region of the shelf wave origin.

Regions of shelf wave occurrence are related to the relatively larger values of the energy flux due to resonance interactions. (These larger values are not seen in Figures 6 and 7; the vectors describe only flux direction, not the value.) The energy flux in these regions depicts a complicated pattern. To elucidate this pattern, we magnified results around the Yermak Plateau and the Chukchi Cap for the K_1 wave (Figures 8 and 9). One can distinctly observe the following features: the flux of energy into these regions, enhancement of flux due to resonance effect, rotating gyres of trapped energy, and outflow of energy beyond the regions. This pattern of gyres and meanders seems to be characteristic for the areas of the shelf wave of tidal origin.

To demonstrate behavior of the energy flux at the anti-amphidromic points, we have generalized the pattern occurring at points of maximum sea levels on the corange and cotidal charts. In Figure 10 the region of the sea level (solid lines) dome is depicted. The flux of energy given by vectors always propagates around such a sea level dome. Dashed lines in the figure are representative of the complicated pattern observed in the cotidal lines distribution. This general picture shows that the energy flux of the shelf waves is usually trapped or partially trapped around the sea level domes.

The presence of regions of enhanced velocity changes the process of dissipation of tidal energy. Dissipation of energy does not proceed in a uniform manner over the whole integration domain, but it takes place mainly in the regions of enhanced velocity. To test this assumption let us consider the dissipations due to bottom friction and lateral friction. The rate of energy dissipation for the K_1 wave in the Arctic Basin and Nordic Seas is 7.72×10^{15} erg s^{-1} . About 67% of this energy is dissipated in the regions of enhanced velocity. The dominant region is Spitsbergenbanken (41%). For the O_1 wave the rate of dissipation in the same Arctic Ocean and Nordic Seas is 8.03×10^{14} erg s^{-1} and about 72% of this energy is dissipated in the shelf wave regions. For the O_1 wave the dominant region of dissipation is the Yermak Plateau (48%).

We have dismissed the influence of ice on the diurnal tides because floating ice appears to have negligible effect on tides. However, one reviewer pointed out that ice could have some effect on the diurnal currents in the regions where diurnal tides are close to resonance and therefore sensitive to potentially smaller effects. Ice influences the resonance properties through friction. In shallow water (in winter) the fast ice not only affects the total friction between ice and water but it also changes the bathymetry [Murty, 1985]. The influence of the fast ice is limited to the shallow water areas where depth is less than 30 m. Close to continental shelf the interaction between tides and ice occurs through the friction which is analogous to the bottom friction. Effect of increased bottom friction we have assessed in the Yermak Plateau region only (Z. Kowalik, Modeling of topographi-

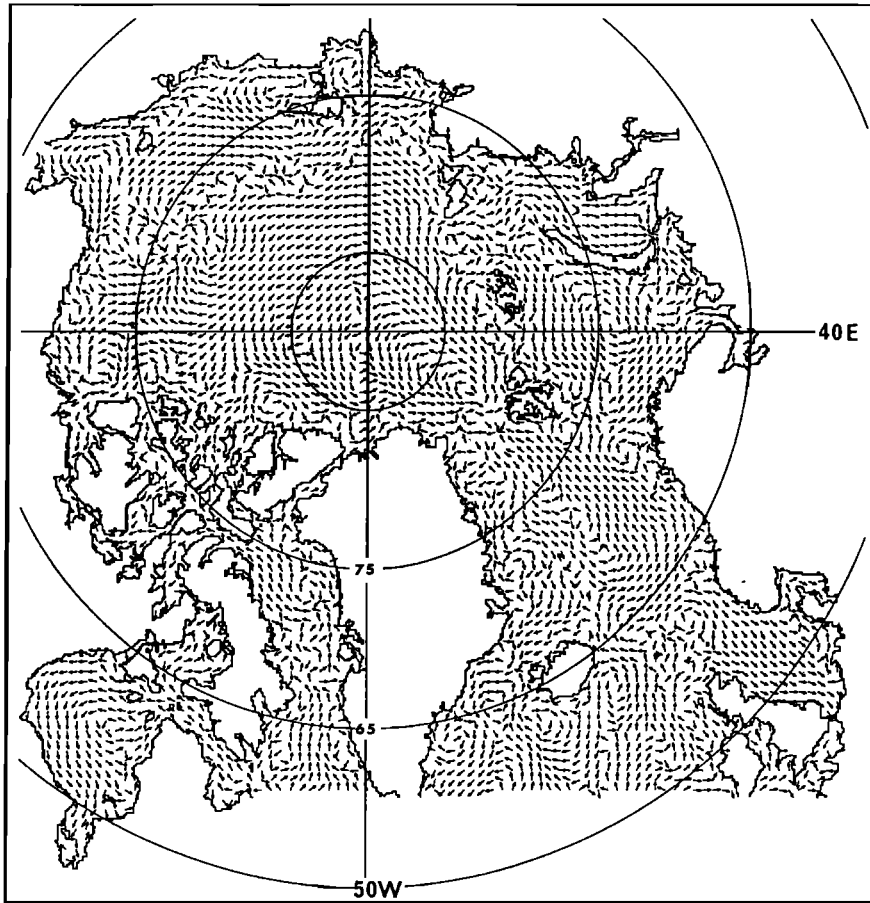


Fig. 6. Tidal energy flux for K_1 wave. Vectors define only direction, not magnitude.

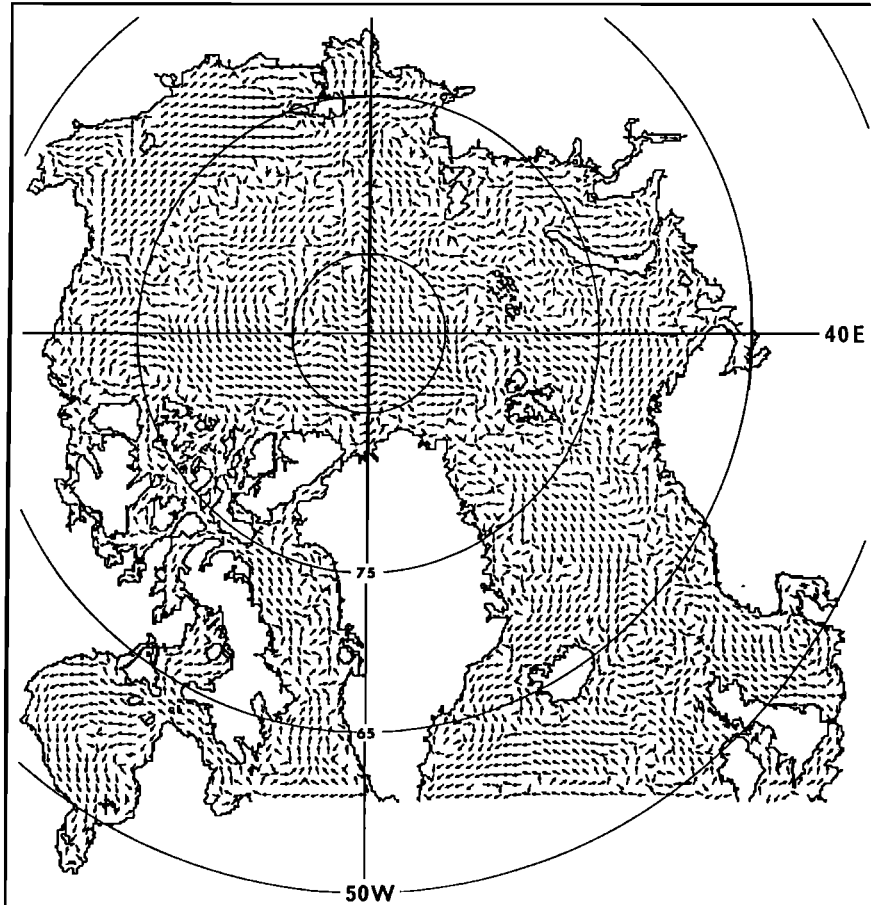


Fig. 7. Tidal energy flux for O_1 wave. Vectors define only direction, not magnitude.

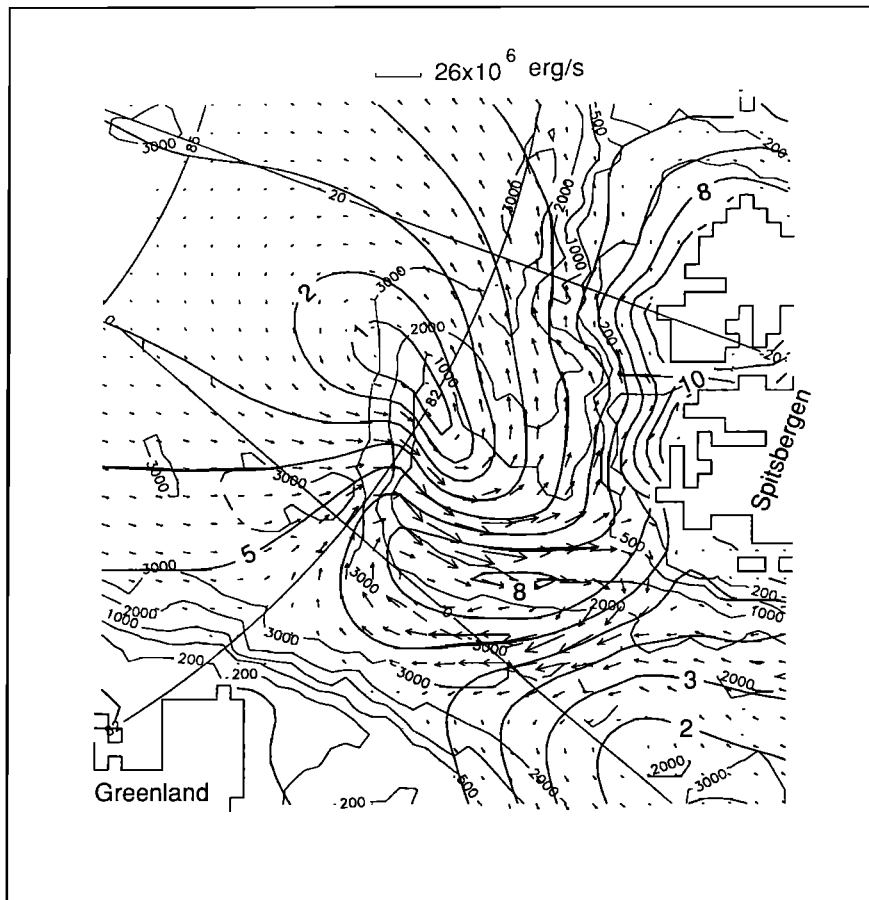


Fig. 8. Tidal energy flux for K_1 wave over the Yermak Plateau region. Vectors define both direction and magnitude. Thin solid lines denote depth contours (in meters). Heavy solid lines denote sea level amplitude (in centimeters).

cally-amplified diurnal tides in the Nordic Seas, submitted to *Journal of Physical Oceanography*, 1993, hereinafter referred to as Kowalik, 1993). Increased friction did not produce any noticeable change in the resonance response at the diurnal period.

5. SUMMARY AND DISCUSSION

We have constructed a tidal model with a resolution of about 14 km, obtained numerical solutions, and analyzed corange, cotidal and ellipse charts in the Arctic Ocean. The conclusion is explicit: the homogeneous "classical" long wave tidal pattern along the continental shelf is often broken by the smaller scale pattern related to shelf waves of tidal origin. These regions require both special measuring and modeling approaches because over a relatively short distance the sea level phase and the currents depict strong variability. In the Arctic Ocean and Northern Atlantic Ocean more than 30 areas of shelf waves were delineated. In these areas a twin system of amphidromic points often exists, probably, as *Cartwright et al.* [1980] suggested, due to superposition of the Kelvin (main tidal wave) with the short shelf wave. In the model calculation, the shelf wave regions depict enhanced tidal currents, located between amphidromic and anti-amphidromic points. An anti-amphidromic point (maximum sea level amplitude) is a region which traps tidal energy. This has been elu-

cidated by the charts of tidal energy flux. The pattern of the energy flux suggests that the shelf waves are trapped or partially trapped by the irregularities of the bottom topography. One can see that the presence of the shelf waves should change the energy flow in the diurnal tidal waves. First, the energy is directed to the regions of shelf wave generation, and second, in these regions the energy is dissipated much stronger than in the surrounding areas.

Do measurements provide a suitable test for shelf waves of tidal origin? We have compared computations against about 200 coastal and pelagic tide gauges. The computed elevations turned out to be in satisfactory agreement with those obtained from observations. It seems, however, that the coastal data do not provide a suitable test for the shelf waves, because these waves occur in the open ocean close to the continental slope. Currently, at least three regions included in the integration domain have been confirmed through measurements to have enhanced velocity or increased sea level in the open ocean along the shelf-continental slope area. Two regions are located in the North Atlantic at St. Kilda shelf [*Cartwright*, 1969; *Cartwright et al.*, 1980] and at Rockall Bank [*Huthnance*, 1974]. The third region located over the Yermak Plateau was investigated by *Hunkins* [1986] and *Padman et al.* [1992].

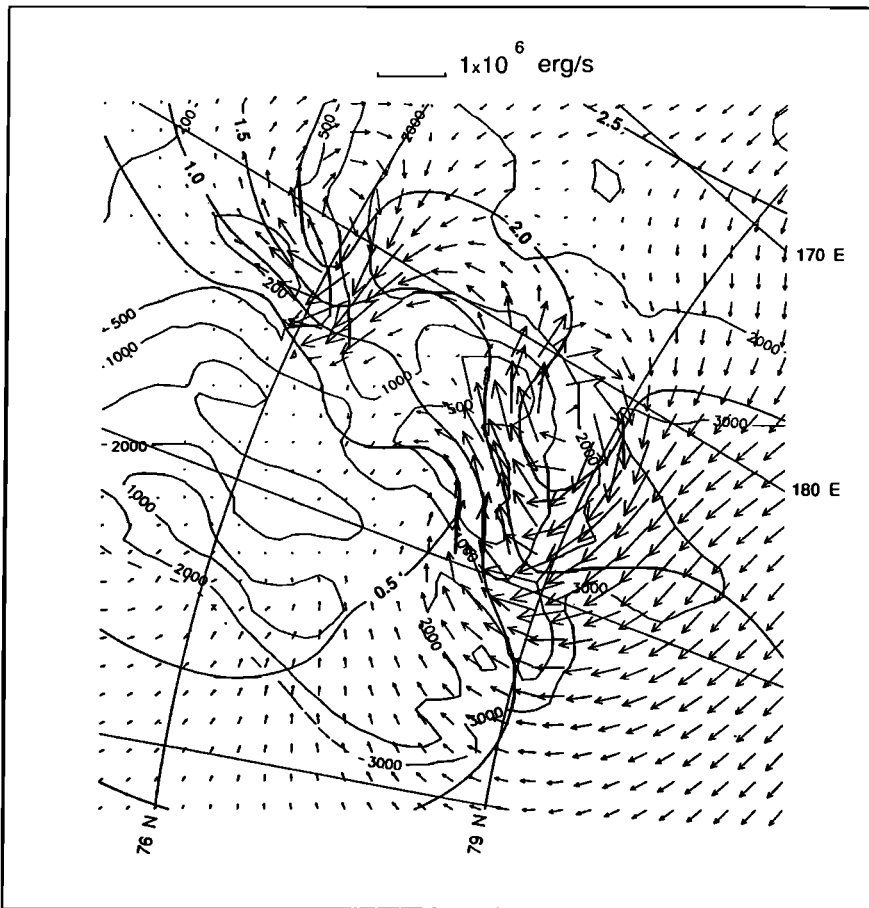


Fig. 9. Tidal energy flux for K_1 wave over the Chukchi Cap region. Vectors define both direction and magnitude. Thin solid lines denote depth contours (in meters). Heavy solid lines denote sea level amplitude (in centimeters).

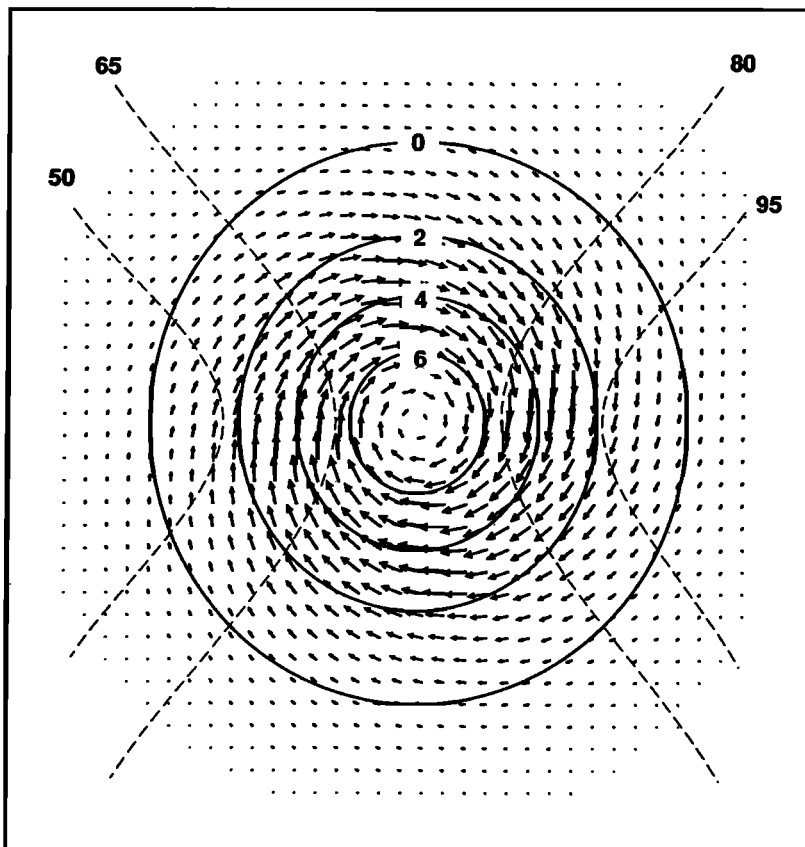


Fig. 10. Characteristic pattern of energy flux (vectors), sea level amplitude (solid lines, in centimeters), and sea level phase (dashed lines, degrees) at the shelf wave region.

Existence of shelf waves in these regions is well confirmed by computations shown in the cotidal, corange, and current ellipse charts.

Kowalik (1993) relates the basic pattern of the current observed over Yermak Plateau, (i.e., strong enhancement and change of the tidal ellipse rotation from clockwise over the Yermak Plateau to counterclockwise at the deep water surrounding Yermak Plateau) to near-resonant interaction of the tides with the local bathymetry.

Acknowledgments. We would like to express our gratitude to R. D. Ray from NASA Goddard Space Flight Center for offering Geosat altimetry data and discussions. We wish to thank N. Z. Cherkis, Naval Research Laboratory, for his advice and data on the bathymetry of the Arctic Ocean. T. Vinje, R. Korsnes, and T. Eiken, Norsk Polar-institutt, Norway, kindly offered their advice and data on the bathymetry and tidal constituents in the Spitsbergen area. We are indebted to L. Padman, Oregon State University, Corvallis, for valuable suggestions and criticism on a draft of this manuscript, and to Chirk Chu, Institute of Marine Science, Fairbanks, for programming help. Reviewers' comments have been helpful in revising the manuscript. We gratefully acknowledge support for this work from the National Aeronautic and Space Administration under grant NAGW-2972 and from National Science Foundation under grant DPP 9114549. Numerical computations were carried out using CRAY Y-MP8/464 from NASA Goddard Space Flight Center.

REFERENCES

- Aagaard, K., L. Darnall, A. Foldvik, and T. Torresen, Fram Strait current measurements 1984–1985, *Rep. 63*, pp. 5–13, Dept. of Oceanogr., Univ. of Bergen, Bergen, Norway, 1985.
- Aagaard, K., C. H. Pease, A. T. Roach, and S. A. Salo, Beaufort Sea mesoscale study, *Outer Cont. Shelf Environ. Assessment Program*, 65, 1–136, 1990.
- Cartwright, D. E., Extraordinary tidal currents near St. Kilda, *Nature*, 223, 928–932, 1969.
- Cartwright, D. E., and B. D. Zetler, Pelagic tidal constants, *IAPSO Publ. Sci.* 33, 59 pp., Int. Assoc. for Phys. Sci. of Oceans, Paris, 1985.
- Cartwright, D. E., J. M. Huthnance, R. Spencer, and J. M. Vassie, On the St. Kilda shelf tidal regime, *Deep Sea Res.*, 27, 61–70, 1980.
- Cartwright, D. E., R. D. Ray, and B. V. Sanchez, Oceanic tide maps and spherical harmonic coefficients from Geosat altimetry, *NASA Tech. Memo.* 104544, 75 pp., 1991.
- Crawford, W. R., Energy flux generation of diurnal shelf waves along Vancouver Island, *J. Phys. Oceanogr.*, 14, 1600–1607, 1984.
- Defant, A., Die Gezeiten des Atlantischen Ozeans und des Arctischen Meeres, *Ann. Hydrog. Mar. Meteorol.*, 52, 153–166, 177–184, 1924.
- Dvorkin, E. N., Tides, in *Soviet Arktik*, Izdatelstvo Nauka, Moscow, pp. 191–197, 1970.
- Fjeldstad, J. E., Results of tidal observations, in *The Norwegian North Polar Research Expedition with the "Maud", 1918–1925*, vol. 4, Scientific Results, pp. 1–88, A S John Griegs Boktrykkeri, Bergen, 1936.
- Francis, O., and P. Mazzega, Global charts of ocean loading effects, *J. Geophys. Res.*, 95, 11,411–11,424, 1990.
- Geophysical Society of America, *Bathymetry of the Barents and Kara Seas*, Boulder, Colo., 1991.
- Gidrographicheskoe Upravlenie VMF SSSR, *Tables of tides* (in Russian), vol. 2, Harmonic constants for tide prediction, 295 pp., Leningrad, 1941.
- Gjevik, B., and T. Straume, Model simulations of the M_2 and the K_1 tide in the Nordic Seas and the Arctic Ocean, *Tellus*, 41, 73–96, 1989.
- Glavnoe Upravlenie po Navigacii i Okeanografii, *Atlas Arktiki*, pp. 22–23, Moscow, 1985.
- Huggett, W. S., M. J. Woodward, F. Stephenson, F. V. Hermiston, and A. Douglas, Near bottom currents and offshore tides, *Beaufort Sea Proj. Tech. Rep.* 16, 38 pp., Ocean and Aquat. Sci., Dept. of Environ., Victoria, B.C., 1975.
- Hunkins, K., Anomalous diurnal tidal currents on the Yermak Plateau, *J. Mar. Sci.*, 44, 51–69, 1986.
- Huthnance, J. M., On the diurnal tidal currents over Rockall Bank, *Deep Sea Res.*, 21, 23–35, 1974.
- Huthnance, J. M., Large tidal currents near Bear Island and related tidal energy losses from the North Atlantic, *Deep Sea Res.*, 28A, 51–70, 1981.
- Hydrographer of the Navy, *Admiralty Tide Tables*, vol. 2, 300 pp., London, 1987.
- Kowalik, Z., A study of the M_2 tide in the ice-covered Arctic Ocean, *Mod., Identif. Control*, 2(4), 201–223, 1981.
- Kowalik, Z., Storm surges in the Beaufort and Chukchi Seas, *J. Geophys. Res.*, 89, 10,570–10,578, 1984.
- Kowalik, Z., and N. Bich Hung, On a system of hydrodynamics equations for certain oceanographical problems in the region of the Earth's pole and the stability of its solution, *Oceanologia*, 7, 5–20, 1977.
- Marchuk, G. I., and B. A. Kagan, *Ocean Tides*, 296 pp., Gidrometeoizdat, Leningrad, 1977.
- McPhee, M. G., Recent measurements of the upper ocean turbulence, draft report, 10 pp., McPhee Res. Co., Naches, Wash., 1991.
- Mooers, C. N. K., and R. L. Smith, Continental shelf waves off Oregon, *J. Geophys. Res.*, 73, 549–557, 1968.
- Morison, J. H., Seasonal variations in the West Spitsbergen Current estimated from bottom pressure measurements, *J. Geophys. Res.*, 96, 18,381–18,395, 1991.
- Muench, R. D., M. G. McPhee, C. A. Paulson, and J. H. Morison, Winter oceanographic conditions in the Fram Strait–Yermak Plateau region, *J. Geophys. Res.*, 97, 3469–3483, 1992.
- Murty, T. S., Modification of hydrographic characteristics, tides, and normal modes by ice cover, *Mar. Geod.*, 9(4), 451–468, 1985.
- Naval Research Laboratory, *Bathymetry of the Arctic Ocean*, Washington, D. C., 1986.

- Norsk Polarinstitutt, *Western Barents Sea Bathymetry*, Oslo, 1989.
- Padman, L., A. J. Plueddemann, R. D. Muench, and R. Pinkel, Diurnal tides near the Yermak Plateau, *J. Geophys. Res.*, *97*, 12,639–12,652, 1992.
- Platzman, G. W., Normal modes of the World Ocean, I, Design of a finite-element barotropic model, *J. Phys. Oceanogr.*, *8*, 323–343, 1978.
- Proshutinsky, A. Y., Tidal water and ice dynamics in the Arctic Ocean, in *Proceedings of the International Conference on the Role of the Polar Regions in Global Change*, vol. 1, pp. 296–303, Geophysical Institute, University of Alaska Press, Fairbanks, 1991.
- Ramming, H. G., and Z. Kowalik, *Numerical Modelling of Marine Hydrodynamics*, 368 pp., Elsevier, New York, 1980.
- Ray, R. D., and B. V. Sanchez, Radial deformation of the Earth by oceanic tide loading, *NASA Tech. Memo. 100743*, 51 pp., 1989.
- Schwiderski, E. W., *Global Ocean Tides, Part IV: The Diurnal Luni-Solar Declination Tide (K_1)*, 87 pp., Naval Surface Weapon Center, Dahlgren, Va., 1981a.
- Schwiderski, E. W., *Global Ocean Tides, Part V: The Diurnal Principal Lunar Tide (O_1)*, 85 pp., Naval Surface Weapon Center, Dahlgren, Va., 1981b.
- Sterneck, R., Die Gezeiten im nördlichen Eismeer, *Ann. Hydr. Mar. Met.*, *56* (21), 1–36, 1928.
- Wahr, J., Body tides on an elliptical, rotating, elastic and oceanless Earth. *Geophys. J. R. Astron. Soc.*, *64*, 677–703, 1981.
- Weber, J. R., and J. F. Sweeney, Reinterpretation of morphology and crustal structure in the central Arctic Ocean basin, *J. Geophys. Res.*, *90*, 663–677, 1985.
- Yefimov, V. V., Y. A. Kulikov, A. B. Rabinovich, and I. V. Fine, *Ocean Boundary Waves*, 280 pp., Gidrometeoizdat, Leningrad, 1985.
- Zahel, W., The diurnal K_1 tide in the world ocean – A numerical investigation, *Pure Appl. Geophys.*, *109*, 8, 1819–1825, 1973.
-
- Z. Kowalik and A.Y. Proshutinsky, Institute of Marine Science, University of Alaska, Fairbanks, AK 99775-1080.

(Received February 2, 1993;
revised May 4, 1993;
accepted May 20, 1993.)